

Induced magneto-conductivity in a two-node Weyl semimetal under Gaussian random disorder

Chuanxiong Xu(徐川雄), Haoping Yu(于昊平), Mei Zhou(周梅), and Xuanting Ji(吉轩廷)

Citation: Chin. Phys. B, 2024, 33 (**9**): 097502. DOI: 10.1088/1674-1056/ad59fc
Journal homepage: http://cpb.iphy.ac.cn; http://iopscience.iop.org/cpb

What follows is a list of articles you may be interested in

Evolution of anomalous Hall effect in ferromagnetic Weyl semimetal $Nb_xZr_{1-x}Co_2Sn$

Bo-Wen Chen(陈博文) and Bing Shen(沈冰)
Chin. Phys. B, 2024, 33 (**8**): 087501. DOI: 10.1088/1674-1056/ad4a3b

Doping-enhanced robustness of anomaly-related magnetoresistance in $WTe_{2\pm\alpha}$ flakes

Jianchao Meng(孟建超), Xinxiang Chen(陈鑫祥), Tingna Shao(邵婷娜), Mingrui Liu(刘明睿), Weimin Jiang(姜伟民), Zitao Zhang(张子涛), Changmin Xiong(熊昌民), Ruifen Dou(窦瑞芬), and Jiacai Nie(聂家财)
Chin. Phys. B, 2023, 32 (**4**): 047502. DOI: 10.1088/1674-1056/acb423

Enhanced and tunable Imbert-Fedorov shift based on epsilon-near-zero response of Weyl semimetal

Ji-Peng Wu(伍计鹏), Yuan-Jiang Xiang(项元江), and Xiao-Yu Dai(戴小玉)
Chin. Phys. B, 2023, 32 (**3**): 037503. DOI: 10.1088/1674-1056/ac7f92

Crystal structure and electromagnetic responses of tetragonal GdAlGe

Cong Wang(王聪), Yong-Quan Guo(郭永权), Tai Wang(王泰), and Shuo-Wang Yang(杨硕望)
Chin. Phys. B, 2020, 29 (**12**): 127502. DOI: 10.1088/1674-1056/abad25

Anomalous Hall effect in ferromagnetic Weyl semimetal candidate $Zr_{1-x}V_xCo_{1.6}Sn$

Guangqiang Wang(王光强), Zhanghao Sun(孙彰昊), Xinyu Si(司鑫宇), Shuang Jia(贾爽)
Chin. Phys. B, 2020, 29 (**7**): 077503. DOI: 10.1088/1674-1056/ab8da8

Induced magneto-conductivity in a two-node Weyl semimetal under Gaussian random disorder

Chuanxiong Xu(徐川雄)[1], Haoping Yu(于昊平)[2], Mei Zhou(周梅)[1], and Xuanting Ji(吉轩廷)[1,3,†]

[1] *Department of Applied Physics, China Agricultural University, Beijing* 100083, *China*
[2] *Department of Applied Mechanics, China Agricultural University, Beijing* 100083, *China*
[3] *School of Physical Sciences, University of Chinese Academy of Sciences, Beijing* 100049, *China*

(Received 20 December 2023; revised manuscript received 20 May 2024; accepted manuscript online 20 June 2024)

Measuring the magneto-conductivity induced from impurities may help determine the impurity distribution and reveal the structure of a Weyl semimetal sample. To verify this, we utilize the Gaussian random disorder to simulate charged impurities in a two-node Weyl semimetal model and investigate the impact of charged impurities on magneto-conductivity in Weyl semimetals. We first compute the longitudinal magnetic conductivity and find that it is positive and increases proportionally with the parameter governing the Gaussian distribution of charged impurities, suggesting the presence of negative longitudinal magneto-resistivity. Then we consider both the intra-valley and inter-valley scattering processes to calculate the induced transverse magneto-conductivity in the model. Our findings indicate that both inter-valley and intra-valley scattering processes play important roles in the transverse magneto-conductivity. The locations of Weyl nodes can also be determined by magneto-conductivity measurements. This is possible if the magnetic field strength and the density of charged impurities are known. Alternatively, the measurement of magnetic conductivity may reveal the distribution of charged impurities in a given sample once the locations of the Weyl nodes have been determined. These findings can aid in detecting the structure of a Weyl semimetal sample, enhancing comprehension of magnetotransport in Weyl semimetals and promoting the development of valley electronics.

Keywords: Weyl semimetal, inter-valley scattering, magneto-conductivity

PACS: 75.47.–m

DOI: 10.1088/1674-1056/ad59fc

1. Introduction

Weyl fermions were first introduced by Hermann Weyl in 1928. These fermions are characterized by their chirality and lack of mass. Up to now, no candidates have been found within the standard model of particle. However, it has been discovered that low energy excitations in certain condensed matter systems, known as Weyl semimetals, can realize Weyl fermions. The initial theoretical proposal for the Weyl semimetal occurred in 2011.[1] Subsequently, in 2015, the first authentic Weyl semimetals were achieved within the TaAs family.[2–6] These findings encourage the search for additional candidates of the Weyl semimetal. Other materials, such as $YbMnBi_2$ (type-I),[7] $Mo_xW_{1-x}Te_2$ (type-II),[8–10] and $(TaSe_4)_2I$ (type-III),[11] have been demonstrated as viable candidates for Weyl semimetals.

Weyl fermions possess chirality and always appear in pairs. The Weyl fermions in the Weyl semimetal can manifest negative longitudinal magneto-resistance (NLMR).[12–14] This is done by applying an electric field parallel to the direction of a magnetic field in the Weyl semimetal, the Weyl fermions of one specific chirality are pumped to their partner of opposite chirality, according to the no-go theorem.[15] The NLMR, an anomalous transport due to chiral anomalies, has been observed in several experiments.[16–18,20–28] However, positive longitudinal magneto-resistance and NLMR were observed in some experiments,[16] indicating that magneto-conductivity measurements are sample-dependent, especially disorder-dependent.[17] Additionally, in weak magnetic fields, some experiments have shown a peak-like nonparabolic negative magneto-resistance.[18,19] Theoretical explanations are needed for these experimental phenomena.

Theoretically, conductivity can be viewed as the collision process between impurity electrons and system electrons near the Fermi energy level. For the undoped case of Weyl semimetal, the Fermi energy level is situated at the Weyl nodes.[1,29,30] The charged impurities introduce additional charges to the energy bands, causing a shift in the Fermi level away from the Weyl nodes. Thus, the Fermi energy levels exhibit extensive variation among the diverse samples evaluated in experiments and are highly responsive to alterations in sample properties. To accurately reproduce and predict experimental results in theoretical calculations, one must consider the diverse distributions of impurities present. There are a large number of theoretical studies[14,31–43] and several studies have examined the impact of distant disorder on the density of states in a weak magnetic field,[31] as well as the density of the states, Landau level broadening, and magneto-resistivity in a transverse magnetic field with short-range or charged impurities.[32] However, most of these studies are based on the one-node model, which assumes the existence of only a

†Corresponding author. E-mail: jixuanting@cau.edu.cn

© 2024 Chinese Physical Society and IOP Publishing Ltd

single Weyl fermion.[31–35] A one-node model cannot present the chiral anomaly because the chiral anomaly requires at least one pair of Weyl fermions. Therefore, studying NLMR in one-node models is not enough.

The two-node model for a Weyl semimetal is the simplest extension of the one-node model. It consists of two Weyl fermions with opposite chirality, allowing for the study of the chiral anomaly. Additionally, two-node model naturally introduces the valley degree of freedom of the Weyl fermion, allowing for the simultaneous study of inter-valley and intra-valley scattering processes. As pointed out in Refs. [44–47], the inter-valley scattering processes contribute significantly to the magneto-conductivity in the presence of an impurity distribution that obeys a screened Coulomb potential or a Dirac δ potential. Furthermore, the magneto-conductivities of the Weyl semimetal are found to be influenced by the distribution of the impurity, which allows for a more precise understanding of the sample dependence of the NLMR.[44,45] However, the screened Coulomb disorder and the Dirac δ potential may not accurately replicate the charged impurities in practical scenarios. Therefore, we propose that the impurities follow a Gaussian distribution. This distribution may provide a more accurate representation of the distribution of charged impurities and model a more realistic Weyl semimetal sample, which is used in experiments. In Ref. [41], the authors studied the longitudinal magneto-resistance induced by charged impurities in a two-node model Weyl semimetal. They modeled the potential of the charged impurities as a random Gaussian potential. They studied the longitudinal magneto-resistance in a two-node model Weyl semimetal using a random Gaussian potential to simulate charged impurities. However, they did not provide details on transverse magneto-conductivity or address inter-valley scattering.

With all of the backgrounds mentioned above, In this work, we utilized a random Gaussian potential, which is more appropriate for the general case, to model the distribution of charged impurities in a two-node Weyl semimetal model. Taking into account the contributions from inter-valley scattering processes, we studied both longitudinal and transverse magneto-conductivity. Based on the calculation of the longitudinal conductivity, it is evident that the conductivity is positive definite and increases with magnetic flux density, indicating the presence of NLMR, supporting the theoretical prediction of chiral anomalies. The results of the transverse magneto-conductivity show that the inter-valley scattering process has nonnegligible contributions to the magneto-conductivity. Furthermore, we carefully analyzed the impact of the length scale of the Gaussian distribution, magnetic field strength, and the position of Weyl nodes on transverse magneto-conductivity. We find that the transverse magneto-conductivity is inversely proportional to the magnetic flux density. In addition, by adjusting the magnetic flux density and the length scale of the Gaussian distribution in our model, we can obtain the cusp-like behavior of the transverse magneto-conductivity of the Weyl semimetal. This differs from the peak caused by the weak localization. The difference between these two mechanisms requires further investigation and will be addressed in a future study. Our results indicate that the peaks are located near the Weyl nodes, so it is possible to infer the structure of a Weyl semimetal sample just by measuring its magneto-conductivity, which may be verified in future experiments.

This paper is organized as follows. In Section 2, we review a two-node model of the Weyl semimetal and present the eigenenergy as well as the eigenstates. In Subsection 3.1, we interpret a mechanism for shifting Fermi energies. Then, we derive the formulas and show the numerical results for the longitudinal and transverse magneto-conductivity in Subsections 3.2 and 3.3. Possible applications of magnetic conductivity measurement are discussed in Subsection 3.4. Section 4 is devoted to conclusions and discussions.

2. A two-node model of the Weyl semimetal

In this section, we will review a two-nodes model for the Weyl semimetal raised in Refs. [44,45], in the absence of an external magnetic field, the Hamiltonian of the two-nodes model can be written as

$$\mathcal{H} = \nu\hbar v_{\mathrm{F}}[(\boldsymbol{k} + \nu\boldsymbol{k}_{\mathrm{c}})\cdot\boldsymbol{\sigma}]. \tag{1}$$

The energy spectrum of Eq. (1) spreads in momentum space with two valleys corresponding to two Weyl nodes with opposite chiralities, we use ν to indicate this with $\nu = 1$ for K valley and $\nu = -1$ for K' valley. $\hbar$ is reduce Planck constant, v_{F} is Fermi velocity. $\boldsymbol{k}_{\mathrm{c}} = (0, 0, \pm k_{\mathrm{c}})$ in momentum space represent the positions of the two nodes. In the following, we will write Eq. (1) into two parts, each part corresponds to one valley:

$$\tilde{H}_K = \mathcal{H}_K - \hbar v_{\mathrm{F}}\boldsymbol{k}_{\mathrm{c}}\cdot\boldsymbol{\sigma}, \tag{2}$$

$$\tilde{H}_{K'} = \mathcal{H}_{K'} - \hbar v_{\mathrm{F}}\boldsymbol{k}_{\mathrm{c}}\cdot\boldsymbol{\sigma}. \tag{3}$$

These two Hamiltonians allow for a more intuitive study of intra-valley and inter-valley scattering processes. We will give their eigenstates and eigenenergies in the following.

For the K valley, the eigenenergies are

$$\tilde{E}_{\pm K} = \pm\hbar v_{\mathrm{F}}\sqrt{{k_x}^2 + {k_y}^2 + {k_z}^2}, \tag{4}$$

with eigenstates

$$\Psi_{+K} = \begin{pmatrix} \cos\frac{\theta}{2} \\ \sin\frac{\theta}{2}\,\mathrm{e}^{\mathrm{i}\varphi} \end{pmatrix}, \quad \Psi_{-K} = \begin{pmatrix} \sin\frac{\theta}{2} \\ -\cos\frac{\theta}{2}\,\mathrm{e}^{\mathrm{i}\varphi} \end{pmatrix}, \tag{5}$$

where $\pm$ represent the conduction and valence bands, respectively. θ and φ are determined as

$$\cos\theta = \frac{k_z}{|\tilde{E}|}, \quad \tan\varphi = \frac{k_x}{k_y}. \tag{6}$$

When a magnetic field $\boldsymbol{B} = (0,0,B)$ is applied along the z-direction, Landau bands form and disperse with k_z. Here we choose the Landau gauge $\boldsymbol{A} = (yB,0,0)$ and we have

$$\boldsymbol{k} = \left(k_x - \frac{eB}{\hbar}y, -\mathrm{i}\partial_y, k_z\right). \tag{7}$$

To obtain the eigenstates, we need to rewrite the Hamiltonian with the ladder operators

$$a = -[(y - {l_B}^2 k_x)/l_B + l_B\partial_y]/\sqrt{2}, \tag{8}$$
$$a^\dagger = -[(y - {l_B}^2 k_x)/l_B - l_B\partial_y]/\sqrt{2}, \tag{9}$$

where $l_B = \sqrt{\hbar/(eB)}$ is the magnetic length. Then Eq. (2) becomes

$$\tilde{H}_K = \hbar v_\mathrm{F}\begin{pmatrix} k_z & -\frac{\sqrt{2}}{l_B}a \\ -\frac{\sqrt{2}}{l_B}a^\dagger & -k_z \end{pmatrix}. \tag{10}$$

Then, the eigenenergies for the original Hamiltonian are

$$E^n_{\pm K} = \tilde{E}^n_{\pm K} + \hbar v_\mathrm{F} k_\mathrm{c}, \tag{11}$$
$$\tilde{E}^n_{\pm K} = \pm\hbar v_\mathrm{F}\sqrt{k_z^2 + 2n/l_B^2}. \tag{12}$$

Here, $n = 0,1,2,\ldots$ is the eigenvalue of the operator $\hat{N} = a^\dagger a$, corresponding to different Landau levels.

Similarly, the corresponding eigenenergies for the K' valley are obtained as

$$E^n_{\pm K'} = \tilde{E}^n_{\pm K'} + \hbar v_\mathrm{F} k_\mathrm{c}, \tag{13}$$
$$\tilde{E}^n_{\pm K'} = \mp\hbar v_\mathrm{F}\sqrt{k_z^2 + 2n/l_B^2}. \tag{14}$$

More details of calculations can be found in the supplementary material.

3. Formalism and results

In this section, we present our main results. In Subsection 3.1, we show how the Fermi energy moves away from the Weyl nodes by adding impurities. We then show the numerical results for longitudinal and transverse and transverse magneto-conductivity in Subsections 3.2 and 3.3. Our main results are presented in Subsection 3.4, where we explain how to determine the structure of a Weyl semimetal sample by measuring its magnetic conductivity.

3.1. The shift of the Fermi energy

In an undoped Weyl semimetal, the Fermi level is located precisely at the Weyl nodes. The addition of donor and acceptor impurities introduces extra charges into the energy bands, shifting the Fermi level away from the Weyl nodes. To illustrate this physical scenario, we define n_d and n_a as the densities of the donor and acceptor, respectively, to calculate the density of excess electrons. With the definition[45]

$$n_\mathrm{imp}(\mu,T) = n_\mathrm{d} - n_\mathrm{a}, \tag{15}$$

the excess electron density is calculated via

$$n_\mathrm{imp}(\mu,T) = g\sum_{\nu=\pm}\sum_{k_z}[f_0(\nu\hbar v_\mathrm{F}k_z - \mu) - f_0(\nu\hbar v_\mathrm{F}k_z)]. \tag{16}$$

Here, $g = 2\times g_0$ represents the spin and Landau level degeneracy, where $g_0 = eB/(2\pi\hbar)$ is the degeneracy of every per unit area. By combine the Fermi–Dirac distribution $f_0(x) = \frac{1}{\mathrm{e}^{x/k_\mathrm{B}T}+1}$, we obtain the excess electron density as

$$n_\mathrm{imp}(\mu,T) = 2g\frac{k_\mathrm{B}T\ln(\frac{\mathrm{e}^{\mu/k_\mathrm{B}T}+1}{2})}{2}. \tag{17}$$

In experiments, the value of n_imp remains constant for each sample containing both donors and acceptors. Hence, by taking $\mu = E_\mathrm{F}$, we obtain the new location of the Fermi energy as (In this paper, we did not consider the effect of temperature. Therefore, in the following calculations, we will fix $T = 3$ K without loss of generality)

$$E_\mathrm{F} \equiv k_\mathrm{B}T\ln\left(2\,\mathrm{e}^{\frac{\pi n_\mathrm{imp}\hbar v_\mathrm{F}}{2gk_\mathrm{B}T}-1}\right). \tag{18}$$

3.2. Longitudinal magneto-conductivity

As the Fermi level leaves the Weyl nodes but does not reach the first Landau level, the transport is essentially involved with the 0-th Landau band. The semiclassical conductivity of this case can be simply figured out by using the Einstein relation $\sigma_{zz} = \mathrm{e}^2 N_\mathrm{F} D$, where $N_\mathrm{F} = (1/(2\pi l_B^2))(2/(\pi\hbar v_\mathrm{F}))$, $D = v_\mathrm{F}^2\tau^{0,\mathrm{tr}}_{k_\mathrm{F}}$ is the diffusion coefficient. $\tau^{0,\mathrm{tr}}_{k_\mathrm{F}}$ is the transport time and k_F is the Fermi wave number. According to semiclassical Boltzmann transport theory, under the first-order Born approximation, for the scattering among the states on the Fermi surface of the 0-th band, we obtain the relaxation time by

$$\begin{aligned}\frac{\hbar}{\tau^{0,\mathrm{tr}}_{k_z}} &= 2\pi\sum_{k_x'k_z'}\langle|U^{0,0}_{k_x,k_z,k_x',k_z'}|^2\rangle\Lambda\,\delta(E_\mathrm{F} - E^0_{k_z'}) \\ &\quad\times(1 - v^z_{0,k_z'}/v_\mathrm{F}),\end{aligned} \tag{19}$$

where E_F is the Fermi energy, and $E^0_{k_z'}$ is the eigenenergy of the 0-th Landau level. $U^{0,0}_{k_x,k_z,k_x',k_z'}$ represent the scattering matrix, it can take place in the scattering process between eigenstate $|0,k_x,k_z\rangle$ and eigenstate $|0,k_x',k_z'\rangle$. $\langle|U^{0,0}_{k_x,k_z,k_x',k_z'}|^2\rangle$ here is the corresponding scattering matrix elements. Λ is introduced to correct the unphysical van Hove singularity near the band edge, which always takes as 1.[44] $v^z_{0,k_z'}$ is the velocity of an electron along the z-direction with the wave number k_z' in the 0-th Landau band. For z-axis magnetic field, we note that only the diagonal elements of the velocity matrix with respect to the z-direction contribute to the longitudinal magneto-conductivity. On the other hand, only the off-diagonal elements of the velocity matrix with respect to the x-direction

contribute to the transverse magneto-conductivity. The longitudinal conductivity σ_{zz} can be found from the formula

$$\sigma_{zz} = \frac{e^2\hbar}{2\pi V}\sum_{k_x,k_z,i} \mathrm{Tr}(\boldsymbol{v}^z_{0,k_z}\boldsymbol{G}^{\mathrm{R}}_{0,k_z}\tilde{\boldsymbol{v}}^z_{0,k_z}\boldsymbol{G}^{\mathrm{A}}_{0,k_z}), \tag{20}$$

both $\boldsymbol{v}$ and $\boldsymbol{G}$ are diagonal matrixes in the valley space, the subscript 0 represents the $n = 0$ Landau subspace.

We defined the $v^{z\boldsymbol{K}}_{0,k_z}$ as the z-direction velocity of an electron in the 0-th band, and $\tilde{v}^{z\boldsymbol{K}}_{0,k_z}$ is the dressed velocity after taking into account the vertex correction. Here we have

$$v^{zK}_{0,k_z} = \partial E^{0K}_{k_z}/\hbar\partial k_z = -v_{\mathrm{F}}. \tag{21}$$

In this case, we fixed the Fermi energy at the 0-th Landau band, and all the Landau bands in the K' cone are fully occupied. Hence, we have

$$\sigma_{zz} = \frac{e^2\hbar}{2\pi V}\sum_{k_x,k_z}(v^z_{0,k_z}\tilde{v}^z_{0,k_z}G^{\mathrm{R}}_{0,k_z}G^{\mathrm{A}}_{0,k_z}). \tag{22}$$

The retarded/advanced Green's function for the 0-th band is $G^{\mathrm{R/A}}_{0\boldsymbol{K}} = 1/(E_{\mathrm{F}} - E^{0K}_{k_z} \pm \mathrm{i}\hbar/(2\tau))$, where τ is the corresponding momentum relaxation time, which is related to the transition probability (induced by the impurities) in K valley at $n = 0$ band. In addition, $V = L_xL_yL_z$ here is the volume of a system.

In the diffusive regime, one can replace $G^{\mathrm{R}}_{0K}\tilde{v}^{zK}_{0,k_z}G^{\mathrm{A}}_{0K}$ by $(2\pi/\hbar)\tau^{0K,\mathrm{tr}}_{k_z}v^{zK}_{0,k_z}\Lambda\,\delta(E_{\mathrm{F}} - E^{0K}_{k_z})$, then we get

$$\sigma_{zz} = \frac{e^2}{V}\sum_{k_z,k_x}(v^{zK}_{0,k_z})^2\tau^{0K,\mathrm{tr}}_{k_z}\Lambda\,\delta(E_{\mathrm{F}} - E^{0K}_{k_z}). \tag{23}$$

To calculate the transport time $\tau^{0K,\mathrm{tr}}_{k_z}$, we need to do the Fourier transform of the Gaussian random potential $f(\boldsymbol{r}) = Ce^{-r^2/2d^2}$, which can be written as

$$U(\boldsymbol{q}) = u_0\, e^{\frac{q^2d^2}{2}}, \tag{24}$$

where u_0 measures the strength, and the parameter d is defined as the range of the scattering potential. After calculating the transport time $\tau^{0K,\mathrm{tr}}_{k_{\mathrm{F}}}$ at the Fermi surface, we obtain the final expression for σ_{zz} as

$$\sigma_{zz} = \frac{2e^2}{h}\frac{(\hbar v_{\mathrm{F}})^2(d^2 + {l_B}^2)}{l_B^2 V_{\mathrm{imp}}\, e^{-(2k_{\mathrm{F}} - k_{\mathrm{c}})^2d^2}}, \tag{25}$$

where $V_{\mathrm{imp}} = n_{\mathrm{imp}}{u_0}^2$, n_{imp} represents the doping degree. The calculation details can be found in the supplementary material.

In Fig. 1, we present the variation of longitudinal magneto-resistance in the two-node model with different Gaussian distribution length scales, described by the parameter d, under the influence of random Gaussian potential doping at low temperature ($T = 3$ K, unless otherwise specified). Consistent with previous studies, we obtained the positive longitudinal magneto-conductivity. Here, we explore the influence of doping on σ_{zz} by varying the parameter d in the impurity potential. The results show that the variation of σ_{zz} with magnetic induction intensity B is linear, which is consistent with the results in Refs. [41,44–46].

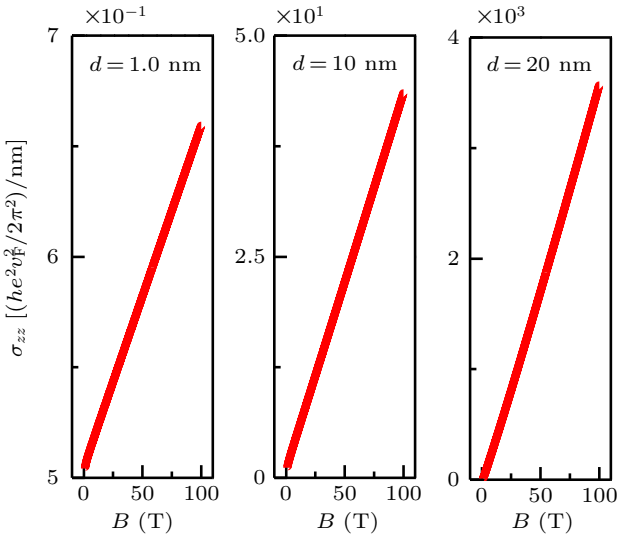


Fig. 1. The longitudinal magneto-conductivity versus the magnetic flux density for different d values. Here $v_{\mathrm{F}} = 10^6$ m/s, $k_{\mathrm{c}} = 0.1$ nm^{-1}, $n_{\mathrm{imp}} = 1.0\times10^{15}$ cm^{-3}.

We further investigate the effect of the length scale of the Gaussian distributions by fixing the value of d at 1.0 nm, 10 nm, and 20 nm, respectively. We find that the longitudinal magneto-resistance increases with increasing d, for d in the range of 0.1 nm to 10 nm the σ_{zz} increases slowly, while for d greater than 10 nm the σ_{zz} increases faster. This phenomenon can be explained by the Heisenberg uncertainty principle, which states that larger impurities with a larger d have a wider distribution, resulting in a smaller change in position (Δx) and a larger change in momentum (Δp). This leads to more intense collision processes and a larger longitudinal magneto-resistance (or smaller longitudinal magneto-conductivity).

3.3. Transverse magneto-conductivity

Similarly, we study in this subsection the transverse magneto-conductivity (σ_{xx}). For consistency, the Fermi energy is assumed to be near the Weyl nodes, and the conductivity along the x-direction can be written as

$$\sigma_{xx} = \frac{e^2\hbar}{2\pi v_{\mathrm{F}}}\sum_{\boldsymbol{k}}\mathrm{Tr}(\boldsymbol{G}^{\mathrm{R}}\boldsymbol{v}^x_{\boldsymbol{k}}\boldsymbol{G}^{\mathrm{A}}\boldsymbol{v}^x_{\boldsymbol{k}}). \tag{26}$$

As in the previous section, both $\boldsymbol{G}$ and $\boldsymbol{v}$ are matrixes, the derivation of Eq. (28) is given in supplementary material, we have

$$\sigma_{xx} = \frac{e^2\hbar}{2\pi v_{\mathrm{F}}}\sum_{k_x,k_z,i,i'}(G^{\mathrm{R}}_{0i}v^x_{0i,i+i'}G^{\mathrm{A}}_{1+i'}v^x_{1+i',0i}). \tag{27}$$

After taking both the intra-valley and inter-valley scatterings into account, we get the total transverse magneto-conductivity

$$\sigma_{xx} = \sigma^K_{xx,\mathrm{inter}} + \sigma^K_{xx,\mathrm{intra}} + \sigma^{K'}_{xx,\mathrm{inter}} + \sigma^{K'}_{xx,\mathrm{intra}}. \tag{28}$$

The relaxation time (τ) corresponding to different scattering processes (two kinds of intra-valley scattering and two kinds of inter-valley scattering) can be listed in supplementary material, and we can get the σ_{xx} by

$$\begin{aligned}
\sigma^{K}_{xx,\mathrm{intra}} &= \frac{e^2}{4\pi^2 h}\frac{V_{\mathrm{imp}}\,\mathrm{e}^{-d^2(2k_{\mathrm{F}}-k_{\mathrm{c}})^2}}{(d^2+l_B^2/2)^2}\frac{F_2^K(k_z)}{4},\\
\sigma^{K}_{xx,\mathrm{inter}} &= \frac{e^2}{4\pi^2 h}\frac{V_{\mathrm{imp}}\,\mathrm{e}^{-d^2 k_{\mathrm{c}}{}^2}}{(d^2+l_B^2/2)}F_1^K(k_z),\\
\sigma^{K'}_{xx,\mathrm{intra}} &= \frac{e^2}{4\pi^2 h}\frac{V_{\mathrm{imp}}\,\mathrm{e}^{-d^2(2k_{\mathrm{F}}-k_{\mathrm{c}})^2}}{(d^2+l_B^2/2)}F_1^{K'}(k_z),\\
\sigma^{K'}_{xx,\mathrm{inter}} &= \frac{e^2}{4\pi^2 h}\frac{V_{\mathrm{imp}}\,\mathrm{e}^{-d^2 k_{\mathrm{c}}{}^2}}{(d^2+l_B^2/2)^2}\frac{F_2^{K'}(k_z)}{4},
\end{aligned}\tag{29}$$

we call Fs form factors, and derive them in supplementary material.

In Fig. 2, we show the variation of the transverse magneto-conductivity as a function of the magnetic induction intensity B for different Gaussian potentials (different parameter ds). To investigate this phenomenon, two characteristic lengths are identified: the potential range, denoted by d, and the magnetic length, designated by l_B. Two distinct regimes can be discerned based on the comparative relationship between these two lengths: the long-range potential regime, where $d \gg l_B$, and the short-range potential limit, where $d \ll l_B$. The magnetic length is $l_B = \sqrt{\hbar/(eB)} \approx 25.6/\sqrt{B}$ nm; thus, by altering the magnetic field strength, the system may traverse these two distinct regimes.[41] We find that the important change characteristics of the transverse magneto-conductivity are different from those of the longitudinal magneto-conductivity, and the transverse magneto-conductivity decreases with the increase of d, which is just the opposite of the longitudinal magneto-conductivity that will be inhibited with the increase of d. Figures 2(a) and 2(b) demonstrate a minor change in transverse magneto-conductivity when the parameter d is small, whereas Figs. 2(c) and 2(d) exhibit a significant change in transverse magneto-conductivity, This is consistent with results in Ref. [41]. Another important feature is clearly shown in the image, under the lower intensity of the magnetic field (0–2 T), the decline trend of the curve is steeper. The appearance of the threshold can be understood as follows: the l_B corresponds to the Landau level degeneracy. When the magnetic field is weak, l_B is large enough to be comparable with the scale of impurity distribution, resulting in more collisions between electrons and charged impurities. When the magnetic field flux exceeds 2 T, the value of l_B rapidly decreases, causing the electrons to become highly degenerate in a small region. Thus, collisions between electrons and impurities become localized, leading to a slow change in transverse conductivity.

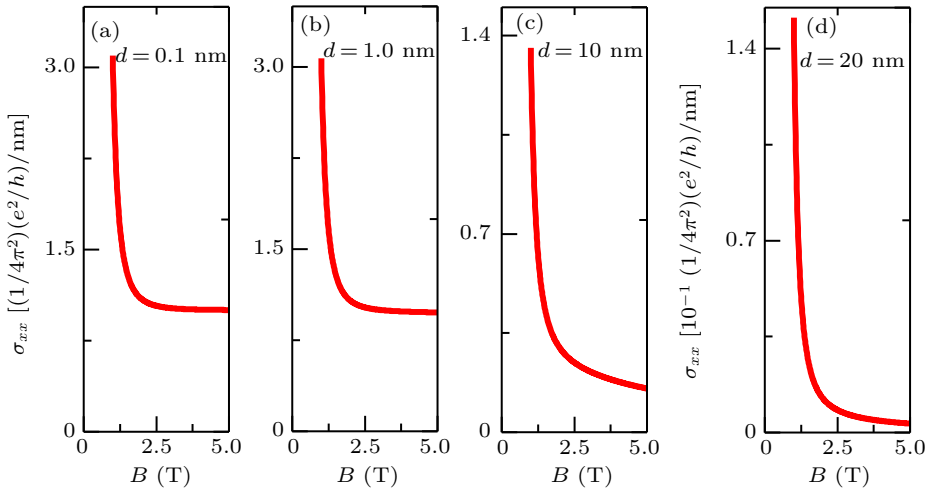


Fig. 2. The transverse magneto-conductivity, σ_{xx}, as a function of B at different d values: (a) $d = 0.1$ nm, (b) $d = 1.0$ nm, (c) $d = 10$ nm, and (d) $d = 20$ nm. Here $k_{\mathrm{c}} = 0.1$ nm^{-1}, $n_{\mathrm{imp}} = 1.0 \times 10^{15}$ cm^{-3}.

In Fig. 3, we further demonstrate the influence of inter-valley scattering on the weight of intra-valley scattering. As shown in Fig. 3(a), the proportion of intra-valley scattering increases with the increase of d value, and when the value of d is large and the magnetic field is weak, intra-valley scattering dominates. In Fig. 3(b), it is observed that as the strength of the magnetic field rises, the value of R, which represents the ratio between the conductivity of the inter-valley scattering process and that of intravally scattering, increases rapidly. This suggests that in order to obtain a more accurate representation of the experiment, the contributions of the inter-valley scattering process on total conductivity must be considered. The proportion of inter-valley scattering reaches a steady state as the magnetic field is increased up to a certain threshold (this corresponds to the case where l_B is almost equal to d). In summary, at weak magnetic fields and small values of d, the intra-valley scattering process dominates. However, under strong magnetic fields and small d, the contributions of the inter-valley scattering process become significant (although the total transverse

conductivity is small).

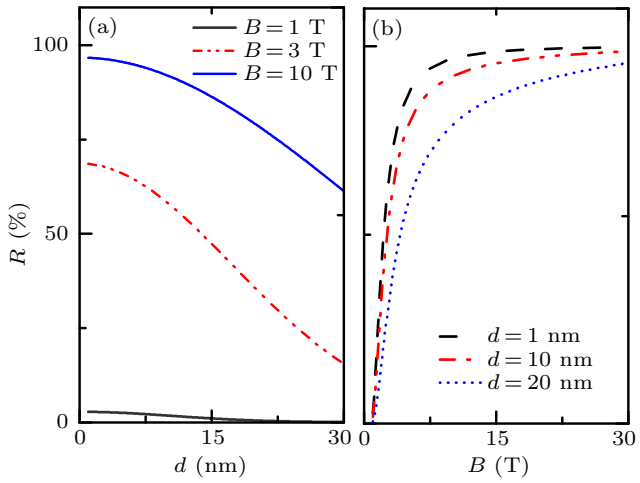


Fig. 3. The trends of ratio R with B and d values are studied. Here, $R=\sigma_{xx,\text{inter}}/\sigma_{xx,\text{intra}}$. Here $k_c=0.1$ nm^{-1}, $n_{\text{imp}}=1.0\times10^{15}$ cm^{-3}.

3.4. Possible application of the measurement of magneto-conductivity

As we can see from Subsections 3.2 and 3.3, the magneto-conductivities induced by the charged impurities are determined by the magnetic field, the location of the Weyl nodes, and the distributions of the impurities. From an experimental perspective, the location of Weyl nodes in an undoped Weyl semimetal crystal sample with a known density of charged impurities may be determined by measuring magneto-conductivity. Conversely, the distribution of charged impurities can be deduced by measuring magneto-conductivity of a doped Weyl semimetal sample in which the Weyl node locations have already been determined. These two cases will be discussed below.

We first consider the case in an undoped Weyl semimetal crystal. As previously stated, the Fermi level shifts due to the introduction of charged impurities. To simulate the distribution of the impurity, we select the length scale $d=1$ nm in Eq. (24) to fix the Fermi level. The density of the impurity is fixed as $n_{\text{imp}}=1\times10^{15}$ cm^{-3}. We adjust the value of k_c and subsequently calculate σ_{xx} based on this impurity distribution. The numerical results are shown in Fig. 4. From Fig. 4(a), it is evident that σ_{xx} displays distinct peaks at different values of k_c and B. As k_c increases, or more precisely, as the distance between two Weyl nodes increases, the value of σ_{xx} decreases. Furthermore, as k_c increases, the peak position shifts to a higher value of B, and the change in σ_{xx} becomes smoother. These results can be understood as follows. As the distance between the nodes increases, the probability of scattering decreases, resulting in a decrease in σ_{xx}. A stronger magnetic field is necessary to increase the probability of scattering and maintain magneto-conductivity. From another perspective, the location of Weyl nodes can be obtained by fixing the value of B. As depicted in Fig. 4(b), if we set $B=1$ T , we can obtain the value of k_c, which is about 0.15497 nm^{-1}. This reminds us that we can use a smooth curve to fit the relationship between k_c (i.e., the locations of the Weyl nodes) and B. Using nonlinear fitting, we obtain the relations as $k_c=\alpha/\left(B^{-\beta}\right)^{\gamma}$, where $\alpha\approx0.15422, \beta\approx2.03193, \gamma\approx0.49202$. By measuring the magneto-conductivity, this equation may be used to determine the location of Weyl nodes in a Weyl semimetal sample with a known density of charged impurities.

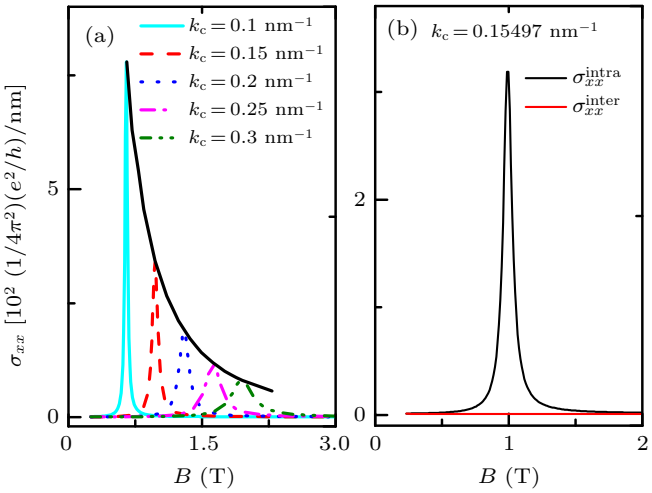


Fig. 4. The transverse magneto-conductivity, σ_{xx}, as a function of B at different k_c (the positions of the Weyl nodes in the momentum space). In (a), the black line is a curve synthesized from the resonance peak. In (b), the black solid line is for intra-valley scattering and the red dashed line is for inter-valley scattering. Here $d=1.0$ nm, $n_{\text{imp}}=1.0\times10^{15}$ cm^{-3}.

As displayed in Fig. 3, the inter-valley scattering process has a significant impact on σ_{xx} and should be considered. To verify this, using the same parameter selection as in Fig. 4(b), Fig. 5 shows only the contributions of the inter-valley scattering process to $\sigma_{xx}^{\text{inter}}$. Compared with the intra-valley behavior $\sigma_{xx}^{\text{intra}}$ shown in Fig. 4(b), numerical results show that these two parts of conductivities have a quite different dependence on weak B. This can be understood as follows: a weak magnetic field corresponds to a relatively larger magnetic length l_B, which leads to l_B being large enough to be compared with the typical scale of the impurity potential d. In the aforementioned circumstances, it is more probable that collisions occur between electrons and charged impurities, resulting in the fact that electrons have a greater likelihood of participating in the inter-valley scattering process. When the magnetic field becomes strong, the l_B decreases rapidly. This causes the electrons to become highly degenerated, ultimately leading to a decrease in conductivity. By calculating the first derivative of the expression for σ_{xx} with respect to B, we confirmed this physical scenario. The numerical results indicate a negative first derivative of σ_{xx} within the ranges of $B=0.2$–0.8 T and $B=1.0$–1.16 T, and a positive first derivative within the ranges of $B=0.9$–1.0 T and $B=1.2$–2.0 T.

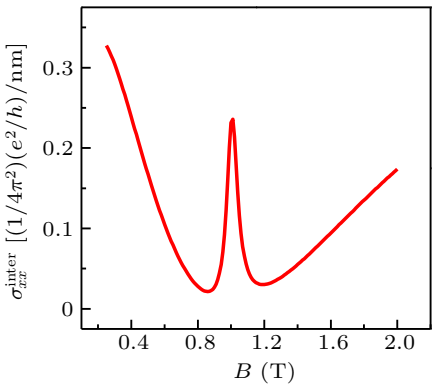


Fig. 5. The inter-valley scattering transverse magneto-conductivity, $\sigma_{xx}^{\rm inter}$, as a function of B. Here, $d = 1.0$ nm, $k_{\rm c} = 0.15497$ nm, $n_{\rm imp} = 1.0 \times 10^{15}$ cm^{-3}.

Now we will compute the magneto-conductivity of a doped Weyl semimetal sample with incomplete information about the impurity distribution. Without loss of generality, we calculate the conductivity σ_{xx} as a function of d and $n_{\rm imp}$ at a fixed magnetic field of $B = 1$ T and $k_{\rm c} = 0.15497$ nm^{-1}. Numerical results are shown in Fig. 6. From Fig. 6(a), we observe that σ_{xx} increases with impurity density $n_{\rm imp}$ and decreases with d. This is caused by the fact that the transverse conductivity σ_{xx}, which describes the transport of carriers along the x-direction driven by a field in the same direction, exhibits insulating properties.[45] The intra-valley process is the primary contributor to the total conductivity, which is increased rapidly with the density of the impurity due to the fact that the high density of impurities increases the probability of hopping between neighbors of the cylindrical orbits of the electrons.[45] On the other hand, for a fixed density of impurity, as the scattering potential range d increases, the impurity will distribute in a relatively large regime, thus the probability of hopping will naturally decrease, resulting in a reduction in σ_{xx}. This scenario is based on intuition, however, in Fig. 6(a) we also observe a disproved outcome. As can be observed when d approaches 10 nm, σ_{xx} becomes smaller with $n_{\rm imp} = 10$ compared to the case with $n_{\rm imp} = 1$. One possible explanation for this phenomenon is as follows: when the typical scale of the impurity potential becomes comparable to the magnetic length l_B, the high density of the impurities indicates the presence of strongly localized scatterers, which may result in the distinct Landau levels beginning to intermingle.[48] Consequently, the electrons of the first Landau level will hop not only to the zeroth order Landau level but also to the other Landau levels. In this work, the conductivity is calculated just by considering the scattering process from the first Landau band to the zeroth Landau band. A more realistic representation may be obtained by considering additional scattering processes of distinct Landau levels, which is beyond the scope of this work. In order to circumvent this potential issue, we have fixed the value of $d = 1$ nm in other parts of the calculation. After comprehending the impact of impurity distribution on conductivity, our attention now turns to how to identify the impurity distribution through magneto-resistivity measurements. Similar as we do in Fig. 4, we calculate the value of σ_{xx} for various $n_{\rm imp}$ while keeping $B = 1$ T, $d = 1$ nm, and $k_{\rm c} = 0.15497$ nm^{-1} fixed. Peaks also appear in σ_{xx} and with a heavy doping, the peaks shift to the right. Similarly, we fit a curve to show the relationship between the impurity density and the magnetic field: $n_{\rm imp} = \eta B^{\lambda}$, where $\eta \approx 1.00501$, $\lambda \approx 0.5$. We may be able to use this property in the experiments to predict the doping level of the sample by measuring the magnetic-conductivity.

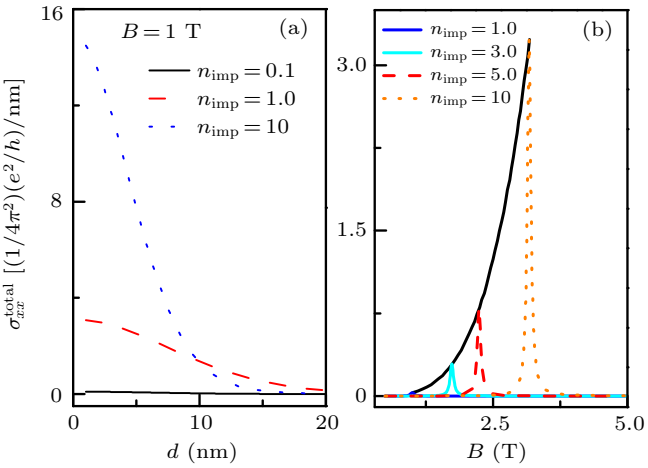


Fig. 6. The transverse magneto-conductivity, $\sigma_{xx,}$, as the functions of d and B at different $n_{\rm imp}$ (represent the doping degree). In (a), the black solid line is for $n_{\rm imp} = 0.1 \times 10^{15}$ cm^{-3}, the red dashed line is for $n_{\rm imp} = 1.0 \times 10^{15}$ cm^{-3}, and the blue dotted line is for $n_{\rm imp} = 0.1 \times 10^{15}$ cm^{-3}, respectively. Here $B = 1$ T. In (b), the blue line is for $n_{\rm imp} = 0.1 \times 10^{15}$ cm^{-3}, the cyan solid line is for $n_{\rm imp} = 3.0 \times 10^{15}$ cm^{-3}, the red dashed line is for $n_{\rm imp} = 5.0 \times 10^{15}$ cm^{-3}, and the orange dotted line is for $n_{\rm imp} = 10 \times 10^{15}$ cm^{-3}, respectively. The black solid line is a curve synthesized from the formant. Here $d = 1.0$ nm, $k_{\rm c} = 0.15497$ nm^{-1}.

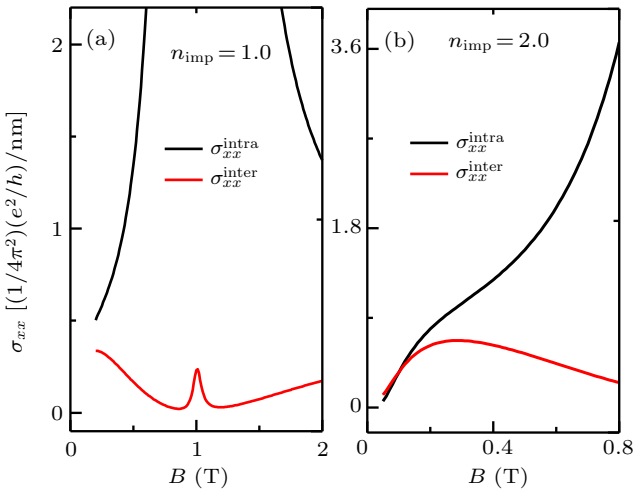


Fig. 7. The transverse magneto-conductivity, $\sigma_{xx}^{\rm intra}$ (the black line) and $\sigma_{xx}^{\rm inter}$ (the red line), as function of B. The densities of the impurities are $n_{\rm imp} = 1.0 \times 10^{15}$ cm^{-3} in (a) and $n_{\rm imp} = 2.0 \times 10^{15}$ cm^{-3} in (b), respectively. Here, $d = 1.0$ nm, $k_{\rm c} = 0.15497$ nm^{-1}.

Finally, we continue to check the contributions to the σ_{xx} from the intra-valley and the inter-valley scattering process.

We calculate σ_{xx} as a function of B with fixed value $d = 1.0$ nm and $k_c = 0.15497$ nm^{-1}. The density of impurity is $n_{imp} = 1.0 \times 10^{15}$ cm^{-3} in Fig. 7(a) and $n_{imp} = 2.0 \times 10^{15}$ cm^{-3} in Fig. 7(b). Similar to Fig. 5, there is a marked difference in the dependence of the intra-valley conductivity on the magnetic field strength compared to the inter-valley conductivity. From Fig. 7(a), we observe that at weak magnetic fields, the inter-valley conductivity closely approximates the intra-valley conductivity (Fig. 7(a) is just a part of Fig. 4(b)). When the density of the impurity increases to $n_{imp} = 2.0 \times 10^{15}$ cm^{-3}, it is observed that the inter-valley conductivity exceeds the intra-valley conductivity at $B = 0.1$ T, as shown in Fig. 7(b). These results provide additional evidence that electrons are more likely to engage in inter-valley scattering under weak magnetic field strengths, highlighting the considerable contributions of inter-valley scattering on magneto-conductivity.

4. Conclusion and outlook

A Weyl semimetal sample found in nature usually contains various impurities, making it crucial to understand the structure of a specific sample for both theoretical and practical purposes. Measuring the magneto-conductivity resulting from impurities may aid in determining the distribution of impurities and revealing the structure of a Weyl semimetal sample. Based on this, we investigate the magneto-conductivity properties of a Weyl semimetal with two Weyl nodes. We employ a Gaussian random potential to model the impurity distribution and analyze the effect of charged impurities on both the longitudinal and transverse magneto-conductivities.

By calculating the longitudinal magneto-conductivity, a definite positive correlation between magnetic flux density and the longitudinal magneto-conductivity is obtained. This suggests the presence of NLMR observed in the experiments. Furthermore, the longitudinal magnetic conductivity is affected by the length scale parameter of the impurity distribution (d). The study reveals that an increase in d enhances the longitudinal magnetic conductivity, and when d reaches a certain threshold (say 10 nm in Fig. 1) the longitudinal magnetic conductivity increases rapidly. These results may explain why negative magneto-resistivity has not been observed in experiments on each Weyl semimetal sample. Due to the varying distribution of impurities in a Weyl semimetal sample, certain distributions may result in a low longitudinal magnetic conductivity, which may become masked by other conductivities.

We then calculate the transverse magneto-conductivity by incorporating the contributions from both the intra-valley and inter-valley scattering processes. We find that the transverse magneto-conductivity is inversely proportional to the magnetic flux density. The inter-valley process becomes significant at a small distribution length scale of d and a strong magnetic flux density of B. Another important aspect of transverse magneto-conductivity is the presence of peaks, depicted in Figs. 4 and 6. Our calculations demonstrate that these peaks occur in proximity to the location of the Weyl nodes (identified as k_c). The results indicate that determining the position of Weyl nodes is possible by measuring the peak of transverse conductivity in combination with precise data on magnetic field and impurity density distribution. Alternatively, if the Weyl node location is fixed, one can deduce the distribution of impurities by measuring the peak of transverse conductivity with precise data on the applied magnetic field. Combined with the measured longitudinal magnetic conductivity data, one may gain insight into the structure of a natural sample of Weyl semimetal objectively and clearly. Furthermore, the disorder effect is also significant to the spin-1 Weyl fermions.[49] It is also of interest to compare our results, which mainly focus on the spin-1/2 Weyl fermions, with those of the aforementioned study.

As we know, multiple pairs of Weyl nodes exist in Weyl semimetal materials in the real world. In addition, it is possible to realize a state in which a Weyl semimetal coexists with a topological nodal line semimetal.[50] Therefore, it is crucial to investigate the effect of impurities on transport in Weyl semimetals with multiple Weyl nodes or in a topological state where multiple topological phases coexist. Furthermore, the distribution of Weyl nodes and transport properties are also affected by strain. In future research, we will analyze the effects of strain on both one pair and multiple Weyl nodes, with the aim of providing a more accurate and realistic prediction of the structure of a Weyl semimetal sample.

Acknowledgements

We would like to thank Zhengang Zhu and Zhi-Fan Zhang for useful discussions. This work is supported by the National Natural Science Foundation of China (Grant No. 61974162).

References

[1] Wan X G, Turner, A M and Vishwanath A 2011 *Phys. Rev. B* **83** 205101
[2] Weng H M, Fang C, Fang Z, Bernevig B and Dai X 2015 *Phys. Rev. X***5** 011029
[3] Lv B Q, Weng H M, Fu B B, *et al.* 2015 *Phys. Rev. X* **5** 031013
[4] Sun Y, Wu S C and Yan B H 2015 *Phys. Rev. B* **92** 115428
[5] Yang L X, Liu Z K, Sun Y, *et al.* 2015 *Nat. Phys.* **11** 728
[6] Levy A L, Sushkov A B, Liu F G, Shen B, Ni N, Drew, H D and Jenkins G S 2020 *Phys. Rev. B* **101** 125102
[7] Borisenko S, Evtushinsky D, Gibson Q, *et al.* 2019 *Nat. Commun.* **10** 3424
[8] Soluyanov A, Gresch D, Wang Z J, Wu Q S, Troyer M, Dai X and Bernevig B 2015 *Nature* **527** 495
[9] Deng K, Wan G, Deng P, *et al.* 2016 *Nat. Phys.* **12** 1105
[10] Zheng H, Bian G, Chang G Q, *et al.* 2016 *Phys. Rev. Lett.* **117** 266804
[11] Li X P, Deng K, Fu B T, *et al.* 2021 *Phys. Rev. B* **103** L081402
[12] Burkov A A 2014 *Phys. Rev. Lett.* **113** 247203
[13] Gorbar E V, Miransky V A and Shovkovy I A 2014 *Phys. Rev. B* **89** 085126
[14] Son D T and Spivak B Z 2013 *Phys. Rev. B* **88** 104412
[15] Nielsen H B and Ninomiya M 1983 *Phys. Rev. B* **130** 389
[16] Zhang C L, Xu S Y, Belopolski I, *et al.* 2016 *Nat. Commun.* **7** 10735

[17] Takiguchi K, Wakabayashi Y K, Irie H, *et al.* 2020 *Nat. Commun.* **11** 4969
[18] Cohn I A, Zybtsev S G, Orlov A P, *et al.* 2020 *JETP Lett.* **112** 88
[19] Zhang Y, Huang X L, Zhang J L, Gao W S, Zhu X D and Pi L 2022 *Chin. Phys. B* **31** 037102
[20] Wang Z G, Fu Z G, Zhang P and Zhang W 2022 *Phys. Rev. B* **105** 205303
[21] Kawasuso A, Suda M and Murakawa H 2023 *J. Appl. Phys.* **133** 223903
[22] Ahmad A and Sharma G 2021 *Phys. Rev. B* **105** 205303
[23] Zhang N, Cheng B, Li H, Li L and Zeng C G 2021 *Chin. Phys. B* **30** 087304
[24] Wadge A S, Grabecki G, Autieri C, *et al.* 2022 *J. Phys.: Conden. Matter* **34** 125601
[25] Ong N P and Liang S 2021 *Nat. Rev. Phys.* **3** 394
[26] Kundu A, Siu Z B, Yang H and Jalil M 2020 *New J. Phys.* **22** 083081
[27] LaBarre1 P G, Dong L, Trinh1 J, Siegrist T and Ramirez A P 2020 *J. Phys.: Conden. Matter* **32** 02LT01
[28] Shekhar C, Nayak A, Sun Y, *et al.* 2015 *Nat. Phys.* **11** 645
[29] Burkov A A and Balents L 2011 *Phys. Rev. Lett.* **107** 127205
[30] Steiner J F, Andreev A V and Pesin D A 2017 *Phys. Rev. Lett.* **119** 036601
[31] Pesin D A, Mishchenko E G and Levchenko A 2015 *Phys. Rev. B* **92** 174202
[32] Klier J, Gornyi I V and Mirlin A D 2015 *Phys. Rev. B* **92** 205113
[33] Lu H Z, Zhang S B and Shen S B 2015 *Phys. Rev. B* **92** 045203
[34] Lu, H Z and Shen S Q 2015 *Phys. Rev. B* **92** 035203
[35] Sbierski B, Pohl G, Bergholtz E and Brouwer P W 2014 *Phys. Rev. Lett.* **113** 026602
[36] Aji V 2012 *Phys. Rev. B* **85** 241101
[37] Jiang B Y, Wang L J Y, Bi R, *et al.* 2021 *Phys. Rev. Lett.* **126** 236601
[38] Behrends J, Kunst F K and Sbierski B 2018 *Phys. Rev. B* **97** 064203
[39] Yan B H and Felser C 2017 *Annu. Rev. Conden. Ma. P* **8** 337
[40] Zhang T T, Song Z D, Alexandradinata A, *et al.* 2018 *Phys. Rev. Lett.* **120** 016401
[41] Zhang S B, Lu H Z and Shen S Q 2016 *New J. Phys.* **18** 053039
[42] Yokouchi T, Ikeda Y, Morimoto T and Shiomi Y 2023 *Phys. Rev. Lett.* **130** 136301
[43] Yu W W, Liu Y, Fang Y, Ke X L, Liu X, Han Z D and Zhang X M 2023 *Front. Phys.* **11** 1260872
[44] Ji X T, Lu H Z, Zhu Z G and Su G 2017 *AIP Adv.* **7** 105003
[45] Ji X T, Lu H Z, Zhu Z G and Su G 2018 *J. Appl. Phys.* **123** 203901
[46] Shao J M and Yan L J 2019 *AIP Adv.* **9** 045319
[47] Feng L T, Ma T C and Zheng Y S 2020 *J. Phys.: Conden. Matter* **32** 205502
[48] Doucot B and Pasquier V 2008 *The Quantum Hall Effect* (Springer) pp. 23–53
[49] Miao S P,Tu D F and Zhou J H 2023 *Chin. Phys. B* **32** 017502
[50] Ji X T and Sun Y W 2024 *Eur. Phys. J. Plus* **139** 485